PNAS RESEARCH ARTICLE | APPLIED PHYSICAL SCIENCES OPEN ACCESS

Optically controlled single-valley exciton doublet states with tunable internal spin structures and spin magnetization generation

Jiawei Ruan[a,b], Zhenglu Li[a,b,1], Chin Shen Ong[a,b], and Steven G. Louie[a,b,2]

Contributed by Steven G. Louie; received May 6, 2023; accepted June 21, 2023; reviewed by Emmanouil Kioupakis and Li Yang

Manipulating quantum states through light–matter interactions has been actively pursued in two-dimensional materials research. Significant progress has been made toward the optical control of the valley degrees of freedom in semiconducting monolayer transition-metal dichalcogenides, based on doubly degenerate excitons from their two distinct valleys in reciprocal space. Here, we introduce a type of optically controllable doubly degenerate exciton states that come from a single valley, dubbed as single-valley exciton doublet (SVXD) states. They are unique in that their constituent holes originate from the same valence band, making possible the direct optical control of the spin structure of the excited constituent electrons. Combining ab initio *GW* plus Bethe–Salpeter equation (*GW*-BSE) calculations and a theoretical analysis method, we demonstrate such SVXD in substrate-supported monolayer bismuthene—which has been successfully grown using molecular beam epitaxy. In each of the two distinct valleys in the Brillouin zone, strong spin–orbit coupling and C_{3v} symmetry lead to a pair of degenerate 1s exciton states (the SVXD states) with opposite spin configurations. Any coherent linear combinations of the SVXD in a single valley can be excited by light with a specific polarization, enabling full manipulation of their internal spin configurations. In particular, a controllable net spin magnetization can be generated through light excitation. Our findings open routes to control quantum degrees of freedom, paving the way for applications in spintronics and quantum information science.

excitonic effects | 2D materials | first principles | spins

Excitons are bound electron–hole pairs (1, 2). Due to their coupling to photons, superposition of excitons can be initialized and readout by optical means, making them an attractive medium for optical manipulation of quantum degrees of freedom (such as spins) that are embedded in them (3–5). For example, in monolayer transition-metal dichalcogenides (TMDs), two energetically degenerate excitons are located separately at the K and K' valleys in the Brillouin zone (BZ), carrying valley indices. They couple to left- and right-circularly polarized light, respectively (6–10). Valley coherence can be accessed via light polarization, and its flexible manipulation has been achieved through applied magnetic field and optical approaches (11–13).

The rapidly growing family of two-dimensional (2D) materials opens up unprecedented opportunities to study new states of matter (14–17). Recently, a monolayer of bismuth atoms supported by semiconducting silicon carbide (Bi/SiC for short) has been successfully grown using molecular beam epitaxy (MBE) (18). Bi/SiC was reported as a 2D quantum spin Hall insulator with a large topological band gap (18–20). The spin–orbit coupling (SOC) effect in this material is significant (with a strength of around 1 eV), largely exceeding other existing 2D materials. A bismuth monolayer on SiC (as shown in Fig. 1*A*) exhibits a honeycomb structure with two symmetry-related sublattices within a unit cell; meanwhile, inversion symmetry is broken due to strong hybridization with the substrate (18). This structure is distinct from those of monolayer graphene and monolayer TMDs, the other two typical honeycomb-structured materials in the literature. Very recently, excitons were experimentally observed in high-quality Bi/SiC samples, and their resonance energies were found to be in good agreement with ab initio *GW*-BSE calculations (21). Therefore, this 2D material could provide an innovative platform to explore excitons with various forms and their interplay with spins.

In this work, we show that strong SOC and C_{3v} symmetry (within a valley) lead to a type of degenerate exciton states — the single-valley exciton doublet (SVXD) states — with optically addressable internal spin configurations in Bi/SiC, making possible applications in spintronics and quantum information. Through ab initio *GW*-BSE calculations, group theoretic analysis, and pseudo-Bloch functions representations, we show that 1) the two

Significance

Quantum information technology relies heavily on controllable quantum states. Excitons possess essential quantum degrees of freedom, such as spins, that in principle can be optically manipulated for control and readout. The two-dimensional topological insulator, substrate-supported monolayer bismuthene, provides an unprecedented platform to explore the internal spin structure of excitons due to its large spin–orbit coupling. Here, we discover a type of doubly degenerate exciton states—single-valley exciton doublet states—whose constituent holes are identical. We show the internal spin structures in the coherent excitation of such excitons can be directly controlled by light polarization, thus enabling for example tunable spin magnetization generation through excitonic processes. Our work inspires routes to quantum state control and possible applications for spintronics.

Reviewers: E.K., University of Michigan; and L.Y., Washington University in St. Louis.

The authors declare no competing interest.

[1]Present address: Mork Family Department of Chemical Engineering and Materials Science, University of Southern California, Los Angeles, CA 90089.

[2]To whom correspondence may be addressed. Email: sglouie@berkeley.edu.

This article contains supporting information online at https://www.pnas.org/lookup/suppl/doi:10.1073/pnas.2307611120/-/DCSupplemental.

Published July 25, 2023.

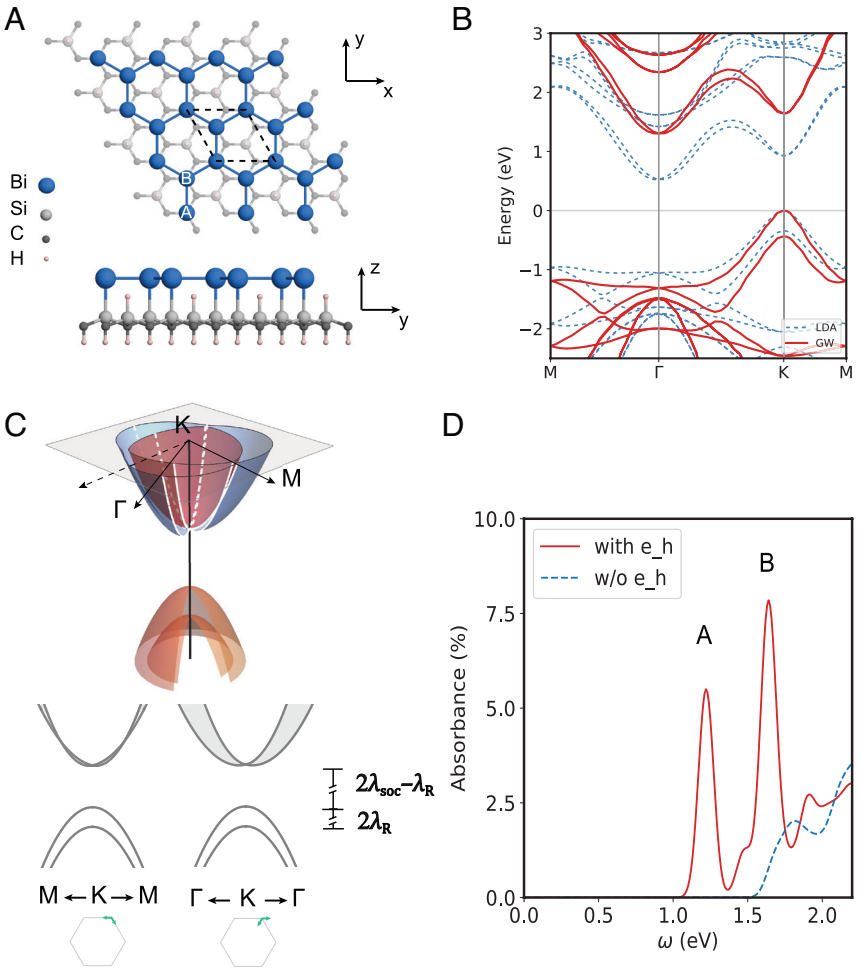

Fig. 1. Crystal structure, electronic structure, and optical absorption spectrum of substrate-supported bismuthene. (*A*) Top and side views of the schematic structure of monolayer bismuthene (blue) on the SiC(0001) substrate (gray). The unit cell is shown by dashed line segments. *A* and *B* sublattices of Bi atoms are indicated. (*B*) Computed DFT-LDA (dashed blue) and *GW* (solid red) band structures. (*C*) Schematic low-energy band structure at the *K* valley. The Rashba splitting of the two conduction bands is anisotropic (the gray filled area). The two conduction bands cross each other along the *K*-*M* direction and remain splitting along the *K*-Γ direction. The **k**-paths for the schematic band structures are denoted by the green arrows. (*D*) Calculated optical absorption spectrum with (red) and without (dashed blue) electron–hole interactions. A Gaussian broadening factor $\sigma = 50$ meV is used. The two main exciton peaks are labeled as A and B.

excitons forming the SVXD arise within a *single* valley and have a 1s-like exciton envelope function; 2) their constituent holes originate from the same valence band and are spin-unpolarized, whereas their constituent electrons are distinct for the two states with opposite spin polarization and sublattice distribution; and 3) they couple to photons with opposite circular polarization of light. Notably, excitation light with a specific polarization can create a coherent superposition state of the SVXD, while controllably configuring its internal spin structure. A net spin magnetization can be generated through excitonic processes and manipulated by varying the polarization and frequency of the incident light.

Fig. 1*A* shows the atomic structure of Bi/SiC used in our first-principles calculations of its electronic and optical properties. This interfacial structure has been successfully realized experimentally and the MBE-grown structure shows no lattice mismatch between the monolayer Bi and the SiC substrate (18). To reduce the computational cost, we use a single layer of SiC to simulate the substrate effect in our calculations, which is shown to accurately capture the low-energy band structure and the physics in this paper (See *SI Appendix* for more details). Fig. 1*B* depicts the Kohn-Sham band structure computed using density functional theory (DFT) in the local density approximation (LDA) as well as the quasiparticle band structure computed using the ab initio *GW* method (22). Both calculations include SOC within the full-spinor formalism. At the K (K') point, the direct gap is 0.93 eV at the DFT level and is 1.64 eV at the *GW* level. There is a large energy splitting between the topmost two valence bands (of 0.43 eV at the *GW* level). In contrast, the bottom-most two conduction bands at the K (K') point are degenerate (see detailed discussion below). The wavefunctions of the states of these four (two conduction and two valence) low-energy bands at K and K' valleys (the two valleys are related by time-reversal symmetry) are basically localized in the bismuth monolayer, with a major contribution from the bismuth p_x and p_y orbitals and a minor contribution from the bismuth s orbital (18).

The significant SOC and substrate effects in this system induce intriguing spin–orbit entangled properties to the low-energy electronic states at the K and K' valleys (19, 23, 24). In the absence of SOC, a graphene-like Dirac gapless dispersion (instead of a gap in the presence of SOC) appears at K (and K') (19, 23). At the Dirac energy point in the case of no SOC, the states at K are composed of orbitals that are p_+^A and p_-^B associated with A and B sublattices of Bi atoms in the honeycomb structure ($p_\pm = \left(\mp p_x - ip_y\right)/\sqrt{2}$). Combining the local on-site orbital angular momentum (± 1 for $p_\pm$) and lattice angular momentum (± 1 for A/B sublattice at wavevector $\mathbf{K}$) together, the p_+^A and p_-^B states carry total orbital angular momenta (in units of $\hbar$) $L_z = \pm 2 \equiv \mp 1 (\mathrm{mod}\ 3)$, respectively (23). Turning on SOC, the electron spins of these basis orbitals mix in and a low-energy Hilbert space of dimension-4 can be constructed. Using the basis of $\left(\left|p_+^A\uparrow,\mathbf{K}\right\rangle, \left|p_+^A\downarrow,\mathbf{K}\right\rangle, \left|p_-^B\uparrow,\mathbf{K}\right\rangle, \left|p_-^B\downarrow,\mathbf{K}\right\rangle\right)$($\uparrow$ / $\downarrow$ denotes spin up/down) with total angular momenta $J_z = 5/2, 3/2, -3/2, -5/2$, respectively, the effective low-energy Hamiltonian at K reads (23)

$$H^{\mathrm{SOC}}(\mathbf{K}) = \begin{pmatrix} \lambda_{\mathrm{SOC}} & 0 & 0 & 0 \\ 0 & -\lambda_{\mathrm{SOC}} & -\mathrm{i}\,\lambda_{\mathrm{R}} & 0 \\ 0 & \mathrm{i}\,\lambda_{\mathrm{R}} & -\lambda_{\mathrm{SOC}} & 0 \\ 0 & 0 & 0 & \lambda_{\mathrm{SOC}} \end{pmatrix}, \quad [1]$$

where λ_{SOC} is an on-site SOC matrix element and is positive, making $|p_+^A\uparrow,\mathbf{K}\rangle$ and $|p_-^B\downarrow,\mathbf{K}\rangle$ to be the conduction band states with the same energy, as well as making the linear combinations of $|p_+^A\downarrow,\mathbf{K}\rangle$ and $|p_-^B\uparrow,\mathbf{K}\rangle$ to be valence band states. λ_{R} (a real number) originates from a Rashba-type SOC, induced by an out-of-plane effective electric field generated from the SiC substrate, and mixes $|p_+^A\downarrow,\mathbf{K}\rangle$ with $|p_-^B\uparrow,\mathbf{K}\rangle$. Thus, the two valence eigenstates at $\mathbf{K}$ take the form of $(|p_+^A\downarrow,\mathbf{K}\rangle \pm i|p_-^B\uparrow,\mathbf{K}\rangle)/\sqrt{2}$. We emphasize that the two topmost valence states are split in energy, whereas the bottom two conduction states remain degenerate, which is guaranteed by the C_{3v} symmetry at the K point. This band arrangement hosts unique exciton structures as will be discussed below. Using time-reversal (TR) symmetry, the band states at K' can be obtained, with $|p_-^A\downarrow,\mathbf{K}'\rangle$ and $|p_+^B\uparrow,\mathbf{K}'\rangle$ as the two degenerate conduction band states and $(|p_+^B\downarrow,\mathbf{K}'\rangle \mp i|p_-^A\uparrow,\mathbf{K}'\rangle)/\sqrt{2}$ as the two split valence band states, which is equivalent to switching A and B sublattice notations of the states at K. Away from the K/K' points, a $\mathbf{k}$-dependent Rashba SOC effect (23) leads to a small but anisotropic Rashba-type splitting in the energy of the two conduction bands (Fig. 1*C*). This splitting is much smaller than the band gap, but it leads to a spin character mixing of the conduction band states near the K/K' points. Here, we emphasize that, the single-valley exciton doublet states we discuss below is formed by the degenerate states within a single individual valley. The photoresponse of excitons in the K and K' valleys (TR-related) are identical, and the whole system follows the single-valley physics.

By directly diagonalizing the first-principles *GW*-BSE Hamiltonian (25, 26), a series of exciton states (their energies and wavefunctions) are obtained with detailed information on their wavefunction character. The ab initio computed optical absorption spectrum for linearly polarized light for our system, including electron–hole interaction (excitonic) effects, is displayed in Fig. 1*D* (red solid curve) as compared to the non-interacting-particle result (blue dashed curve). There are two main peaks, denoted as A and B, with excitation energies of 1.22 eV and 1.64 eV, respectively. Peak A (B) corresponds to the excitation of the lowest-energy optically bright exciton states that are mainly formed by interband transitions between the first (second) valence band and the two degenerate conduction bands. The excitons from both valleys (related by TR symmetry from each other) contribute to the peaks for this case of linearly polarized light.

We now investigate in detail the character of the SVXD in one specific valley, which is allowed because the coupling between K and K' valleys is negligible (~0.1 meV; *SI Appendix*). We focus on the A-series exciton properties in the K valley. Fig. 2*A* shows the energies and optical selection rules of the exciton states for linearly polarized light. To characterize their symmetry properties and degeneracies, we developed a method to directly calculate the group representations for the exciton states (See *SI Appendix* for the details). The irreducible representations under C_{3v} symmetry for several of the low-energy excitons are shown in Fig. 2*A*.

The lowest two excitons $|1s_+\rangle$ and $|1s_-\rangle$ of the K valley are degenerate, corresponding to $\mathbf{e}_+$ and $\mathbf{e}_-$ chirality, respectively, where $\mathbf{e}_\pm$ are defined as $(\mp\mathbf{e}_x - \mathbf{i}\mathbf{e}_y)/\sqrt{2}$ with $\mathbf{e}_x$ ($\mathbf{e}_y$) denoting the unit vector along the $+x$ ($+y$) direction, defined in a global coordinate system (Fig. 1*A*). The nature of these excitons, however, can be obscured by the direct numerical diagonalization from the *GW*-BSE calculations, which contains challenges associated with the random phases and mixing of degenerate states (*SI Appendix*). To solve this problem, we adopt the concept of pseudo-Bloch functions (27) (denoted as $|\chi_{m,\mathbf{k}}\rangle$ for the single-particle orbitals, which is a symmetrized combination of Bloch states at a given $\mathbf{k}$ point as shown in Fig. 2*B*). They serve as a different kind of basis of electron and hole states with a smooth gauge to give unambiguous representations of the internal structure of exciton states. The constructed two pseudo-Bloch conduction band states $|\chi_{c1,\mathbf{k}}\rangle$ and $|\chi_{c2,\mathbf{k}}\rangle$ have main character of $p_+^A\uparrow$ (denoted as $\Uparrow$) and $ip_-^B\downarrow$ (denoted as $\Downarrow$), respectively. These pseudo-Bloch conduction band states have spins that are locked with sublattice indices and angular momentums, which inherit the properties of the states at the K point. The energy bands depicted in Fig. 2*B* for the pseudo-Bloch states are defined as the expectation value of these constructed states with respect to the quasiparticle Hamiltonian.

In the pseudo-Bloch basis, the degenerate exciton states of the A series can be expressed as $|1s_\pm\rangle = \Sigma_{\mathbf{k}} C_1^{1s_\pm}(\mathbf{k})|\chi_{v\mathbf{k}}^*;\chi_{c1,\mathbf{k}}\rangle + \Sigma_{\mathbf{k}} C_2^{1s_\pm}(\mathbf{k})|\chi_{v\mathbf{k}}^*;\chi_{c2,\mathbf{k}}\rangle$, where $C_i^S(\mathbf{k})$ are the envelope functions in this constructed basis (see *SI Appendix* for details), as shown in Fig. 2*D*. We find that the $1s_+$ and $1s_-$ excitons are dominated (>99.7%) by transitions from the topmost valence band to the first and second pseudo-Bloch conduction bands shown as the upper and lower panels in Fig. 2*C*, respectively, with a same *s*-like envelope function in $\mathbf{k}$-space. Thus, they can be simply written as $|1s_+\rangle \approx \Sigma_{\mathbf{k}} f(\mathbf{k})|\chi_{v\mathbf{k}}^*;\chi_{c1,\mathbf{k}}\rangle$ and $|1s_-\rangle \approx \Sigma_{\mathbf{k}} f(\mathbf{k})|\chi_{v\mathbf{k}}^*;\chi_{c2,\mathbf{k}}\rangle$, where $f(\mathbf{k}) \approx C_1^{1s_+}(\mathbf{k}) \approx C_2^{1s_-}(\mathbf{k})$.

The optical selection rules (28, 29) for the SVXD become clear in this basis. Taking the $1s_+$ exciton as an example, the interband velocity matrix elements for its dominant interband transition ($v \to c1$) are related to $\tilde{v}_{v,c1,\mathbf{k}}^{\mp} = \langle\chi_{v,\mathbf{k}}|\mathbf{e}_\mp\cdot\hat{\mathbf{v}}|\chi_{c1,\mathbf{k}}\rangle = \langle\chi_{c1,\mathbf{k}}|\mathbf{e}_\pm\cdot\hat{\mathbf{v}}|\chi_{v,\mathbf{k}}\rangle^* = \left(\tilde{v}_{c1,v,\mathbf{k}}^{\pm}\right)^*$, which correspond to the optical excitation from the top valence band to the first pseudoconduction band illuminated by $\mathbf{e}_\pm$ circularly polarized light, respectively. These matrix elements viewed as a 2D vector field are shown in the upper two panels in Fig. 2*E* for the two circular polarizations. They have winding numbers $l_- = 0$ and $l_+ = 2$, respectively (see *SI Appendix* for more details about choosing the conventions in the winding numbers and the selection rules). Comparing these winding numbers to the angular momentum of the envelope function of the $1s_+$ exciton being $m = 0$, we see for this exciton we have $m = -l_-$ and $m \neq -l_+$. A generalized optical selection rule for excitons in 2D systems is recently derived by Cao, Wu and Louie (CWL) (28) which says that an exciton is optically dark unless $m = -l_\mp \pmod n$ for a material with n-fold rotational symmetry along with sufficient magnitude for velocity matrix elements. Following the CWL selection rule, we can conclude that $|1s_+\rangle$ is strongly optically active under $\mathbf{e}_+$ polarized light and strictly optically inactive under $\mathbf{e}_-$ polarized light. Similarly, the CWL selection rule together with the results in Fig. 2*E* shows that the $1s_-$ exciton is strongly coupled to $\mathbf{e}_-$ polarized light only.

Here, we propose that the singe-valley exciton doublet states and their internal spin configurations can be coherently controlled by optical means because of their optical selection rules and special internal structures noted above. We first introduce the Bloch

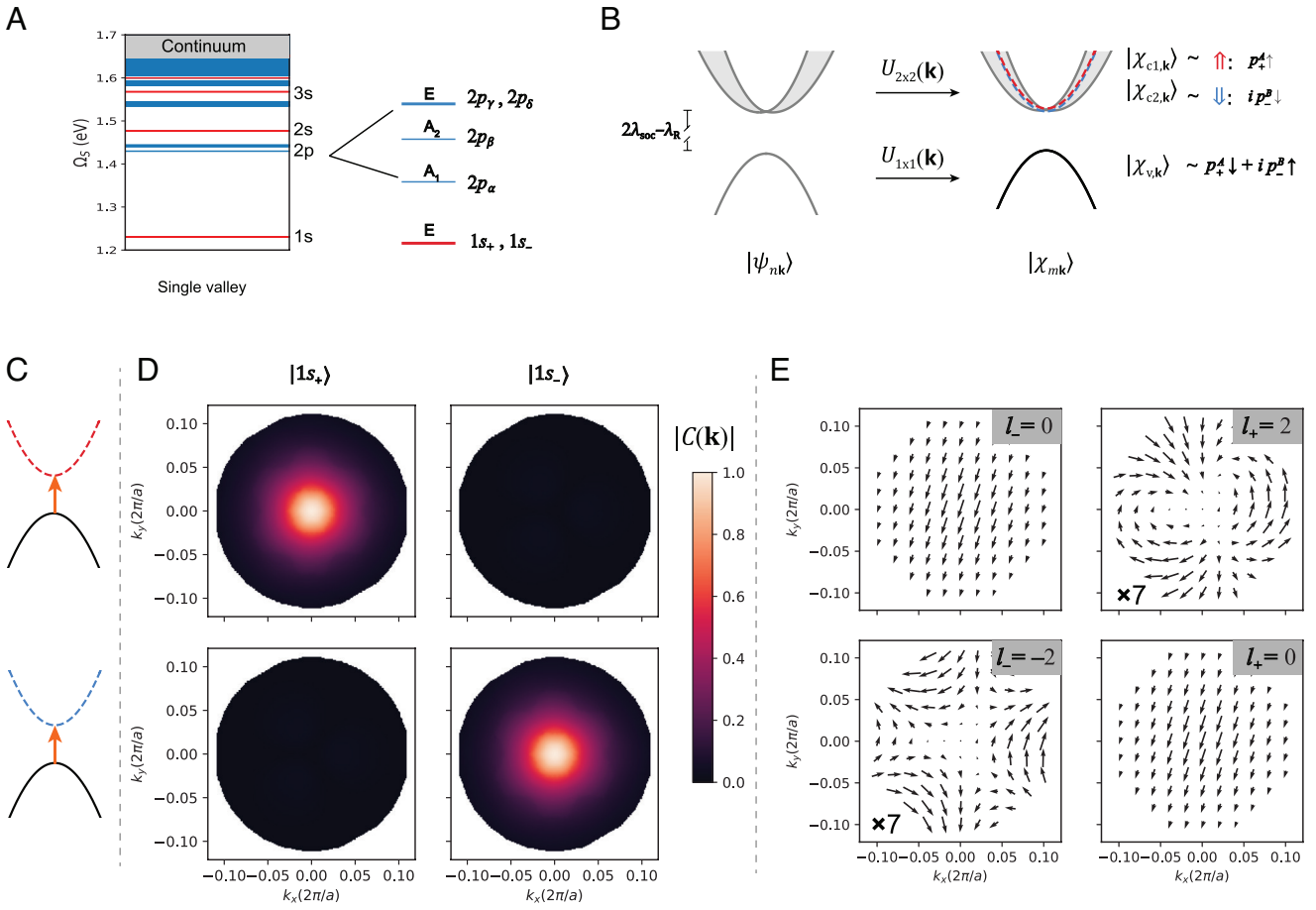

Fig. 2. Exciton envelope functions and interband velocity matrix elements in the pseudo-Bloch basis. (*A*) Single-valley (the K valley as an example) exciton energy levels in the A series. Optically bright (dark) exciton states under linearly polarized light are in red (blue) color. The group representations of the lowest six exciton states are labeled in the right panel. (*B*) Pseudo-Bloch functions $|\chi_{m\mathbf{k}}\rangle$ with smooth gauges, constructed from Bloch eigenfunctions $|\psi_{n\mathbf{k}}\rangle$ of bands that are degenerate at *K* by unitary transformations. The constructed pseudo-Bloch conduction bands are depicted using dashed red and dashed blue curves, with the colors respectively denoting spin-up and spin-down polarizations. The constructed topmost valence band is depicted using a solid black curve. Spin–orbit–sublattice locked characters are shown for each of the pseudo-Bloch bands. For details of the construction method, see *SI Appendix*, section S3. (*C*) Illustration of the two sets of interband transitions in the pseudo-Bloch basis forming the A excitons. (*D*) The absolute value of the amplitude of the envelope functions $C_i^S(\mathbf{k})$ of the excitons $1s_+$ (*Left Top/Bottom* panels) and $1s_-$ (*Right Top/Bottom* panels) in terms of the two pseudo-Bloch band-to-band transitions shown in C (*Top/Bottom* panels). (*E*) The interband velocity matrix elements $v_{v,c;\mathbf{k}}$ in the basis of pseudo-Bloch functions and their winding numbers $l_\mp$. *Upper* (lower) two panels are velocity matrix elements corresponding to interband transitions shown in the *Upper* (lower) panel in C. The direction and length of the arrows denote the phase and magnitude of the matrix elements, respectively. The magnitudes in the lower-left and upper-right panels are multiplied by a factor of 7 for better visibility. For all the k-space plots in *D* and *E*, the *K* point is placed at the origin.

sphere to describe light with a general in-plane polarization such as elliptical polarization (Fig. 3*A*). Given the two-angle parameter $\boldsymbol{\vartheta} = (\theta, \phi)$, the corresponding unit vector of the light polarization is defined as $\mathbf{e}_{\boldsymbol{\vartheta}} = \cos\frac{\theta}{2}\mathbf{e}_+ + \sin\frac{\theta}{2}e^{i\phi}\mathbf{e}_-$. Under illumination of such polarized light, a coherent superposition of the SVXD can be excited in the form of $|1s_{\boldsymbol{\vartheta}}\rangle = \cos\frac{\theta}{2}|1s_+\rangle + \sin\frac{\theta}{2}e^{i\phi}|1s_-\rangle$. Since the basis exciton states $|1s_+\rangle$ and $|1s_-\rangle$ basically share the *same* envelope function and *same* hole states (in the pseudo-Bloch basis), this coherent exciton state can be further expressed as

$$|1s_{\boldsymbol{\vartheta}}\rangle \approx \sum_{\mathbf{k}} f(\mathbf{k}) \left|\chi^*_{v,\mathbf{k}}\right\rangle \otimes |\chi_{c,\mathbf{k}}(\boldsymbol{\vartheta})\rangle, \qquad [2]$$

with $|\chi_{c,\mathbf{k}}(\boldsymbol{\vartheta})\rangle = \cos\frac{\theta}{2}\left|\chi_{c1,\mathbf{k}}\right\rangle + \sin\frac{\theta}{2}e^{i\phi}\left|\chi_{c2,\mathbf{k}}\right\rangle$. We can see in this superposition state of the SVXD, the hole part $\left|\chi^*_{v,\mathbf{k}}\right\rangle$ is fixed and independent of the polarization of the incoming photon, whereas the electron part $|\chi_{c,\mathbf{k}}(\boldsymbol{\vartheta})\rangle$ is a coherent superposition of two spin-polarized electron states (*Right* panel in Fig. 3*B*), which is controllable by the incident light polarization (see the schematic in Fig. 3*F*). In other words, the absorbed light information is directly transferred to the excited exciton through its electron component. As a specific illustration, let us take the superposition parameters to be along a fixed longitude of the Bloch sphere in Fig. 3*A* (with $\phi = 0°$ as an example). The one-to-one correspondence between the $\mathbf{e}_{\boldsymbol{\vartheta}}$ polarized light and the superposition state $1s_{\boldsymbol{\vartheta}}$ leads to the prediction that the square modulus of the exciton velocity matrix element $T_{\boldsymbol{\vartheta}} = \left|\left\langle 1s_{\boldsymbol{\vartheta}}\middle|\mathbf{e}_{\boldsymbol{\vartheta}}\cdot\hat{\mathbf{v}}\middle|0\right\rangle\right|^2$ is identical to that of $|1s_+\rangle$ under $\mathbf{e}_+$ polarized light (denoted as T_0) for all parameter choice $\boldsymbol{\vartheta}$, shown as the red line in Fig. 3*D*. At the bottom of Fig. 3*D*, we depict the characters of internal electron (up to a $U(1)$ phase) of four special superposition states that are respectively excitable by light with $\mathbf{e}_+$, $\mathbf{e}_x$, $\mathbf{e}_-$ and $\mathbf{e}_y$ polarizations.

We evaluate the z-direction total spin expectation values $\mathcal{J}_z^{\text{tot}}$ for the superposition states of the SVXD. For the exciton state $|1s_+\rangle$ (with the character $\frac{1}{\sqrt{2}}\left(\left|p_+^A\downarrow\right\rangle + i\left|p_-^B\uparrow\right\rangle\right) \otimes \left|p_+^A\uparrow\right\rangle$) excited by $\mathbf{e}_+$ polarized light, the hole part has zero net spin expectation, and thus $\mathcal{J}_z^{\text{tot}}$ is solely determined by the electron part, which is around $\hbar/2$. Indeed, our first-principles *GW*-BSE calculations give

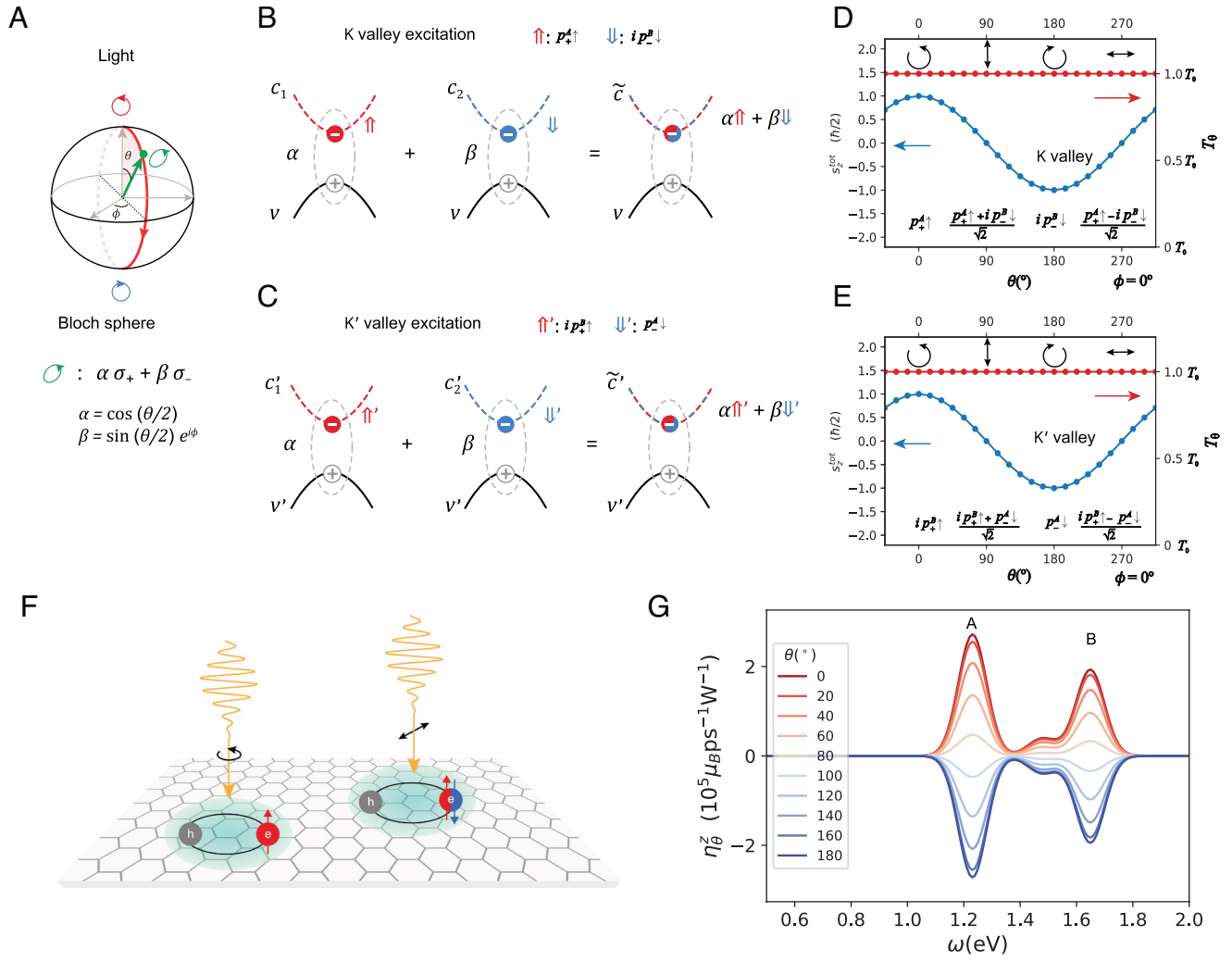

Fig. 3. Optically excited coherent superposition of SVXD states and light controllable generation of spin magnetization. (*A*) General polarization of light characterized by the two-angle parameter $\mathfrak{d} = (\theta, \phi)$, which can be represented by a point (green dot) on the Bloch sphere. (*B*) A coherent superposition of the SVXD states at the *K* valley created by light with the polarization shown in *A*. This coherent exciton state can be equivalently represented as the hole bound to a coherent superposition of two electron states with the same coherent parameter. The spin–orbit–sublattice locked characters (denoted as ⇑ and ⇓) are shown at the top. (*C*) Same as *B* but for states at the *K′* valley. (*D* and *E*) Square modulus of the exciton velocity matrix elements $T_{\mathfrak{d}}$ (red) and the spin expectation values $\mathcal{J}_z^{\text{tot}}$ (blue) of the coherent superposition exciton states at the *K* valley and *K′* valley, respectively. The superposition parameters are chosen to be along the longitude line of the Bloch sphere shown in *A* with $\phi = 0$. Four specific in-plane light polarizations ($\mathbf{e}_+$, $\mathbf{e}_y$, $\mathbf{e}_-$ and $\mathbf{e}_x$ polarizations) and their corresponding excited electron characters (each up to a phase) are depicted. (*F*) Schematic of excitons (and their spin structures) excited by two representative light polarizations, $\mathbf{e}_+$ circularly polarized light (*Left*) and linearly polarized light (*Right*). (*G*) Light-generated spin magnetic moment per picosecond per unit of incident light power $\eta_{\mathfrak{d}}^z(\omega)$ as a function of the polarization and frequency of light. A Gaussian broadening factor $\sigma = 50$ meV is used.

$\mathcal{J}_z^{\text{tot}}(1s_+) = 0.99(\hbar/2)$. This is entirely distinct from monolayer TMDs, where there is no net spin expectation value for exciton created under circularly polarized light. For a general superposition state $|1s_{\mathfrak{d}}\rangle$ with superposition parameter $\mathfrak{d} = (\theta, \phi)$, the spin expectation value is given by $\mathcal{J}_z^{\text{tot}}(1s_{\mathfrak{d}}) = 0.99\cos\theta(\hbar/2)$, depending only on the polar angle θ. We show this spin property of the superposition states along the above-mentioned excitation path in Fig. 3*D*.

The SVXD at the *K′* valley can be controlled in the same manner as those at the *K* valley (Fig. 3*C*). We note that in this valley, the upward spin in the excited electrons is also locked with positive orbital angular momentum (but locked with the *B* sublattice), and it is also excited by $\mathbf{e}_+$ polarized light; and vice versa for the downward spin. Thus, the spin expectation values of the superposition states of SVXD at the *K′* valley are the same as those at the *K* valley for a given light polarization (Fig. 3 *E* and *D*). When optically excited, the two valleys have additive contributions to the spin polarization.

With this knowledge of manipulating the spin configurations of the SVXD, we propose an optical spin generation mechanism and quantitatively estimate the amount of the generated spin magnetization. Let us consider the exciton spin expectation value in the optical absorption process. We define a spin-resolved optical response function, which measures spin magnetic moment created per unit time under illumination of unit power of light. It is given as

$$\eta_{\mathfrak{d}}^z(\omega) = c_\mu \sum_s \sum_{s'} \frac{1}{\omega^2} \langle 0|\mathbf{e}_{\mathfrak{d}}^* \cdot \hat{\mathbf{v}}|S\rangle\langle S'|\mathbf{e}_{\mathfrak{d}} \cdot \hat{\mathbf{v}}|0\rangle\langle S|\hat{\mathcal{J}}_z^{\text{tot}}|S'\rangle D_{s,s'}\delta(\Omega_s - \hbar\omega). \quad [3]$$

where $\hat{\mathcal{J}}_z^{\text{tot}}$ is the z-component of the total spin operator including contributions from the electron and hole in an exciton, Ω_S is the excitation energy of the exciton states $|S\rangle$, C_μ is a constant prefactor, and $D_{S,S'}$ is a function which equals 1 when S and S' are degenerate otherwise vanishes (see *SI Appendix* for more details about the

derivation of Eq. **3** and the constant prefactor C_μ). In Fig. 3*G*, we plot $\eta^z_{\mathfrak{g}}(\omega)$ as a function of the polar angle θ, with ϕ fixed to zero, without loss of generality. A peak appears at the resonance frequency of the A excitons, and the rate of spin magnetization creation is maximal under circularly polarized light and can be continuously tuned by varying the light polarization. Similar behaviors can be found at the resonance frequencies of the B excitons. These characteristic peaks arise because electron–hole interactions give rise to constructive interference of various spin matrix elements, resulting from excitonic wavefunctions being correlated superposition of free electron–hole pair excitations. This effect strongly enhances the light-induced spin magnetization, akin to the excitonic enhancement in the linear optical absorption shown in the Fig. 1*D*. We expect that this controllable spin magnetization can be detected in various photocurrent measurements (30–33).

In summary, through ab initio *GW*-BSE calculations and a pseudo-Bloch function representation method, we have predicted the existence of unique single-valley exciton doublet states whose internal spin configuration can be optically controlled in the 2D topological material Bi/SiC. The tunable spin configuration permits the optical generation and manipulation of net spin magnetization. As they offer an exceptional interface between photons and spins, we anticipate that these degenerate exciton states can pave the way for potential applications in quantum information science and spintronics.

Methods

To determine the ground-state properties, we perform DFT calculations of Bi/SiC using the QUANTUM ESPRESSO package (34). We use norm-conserving pseudopotentials with a plane-wave energy cutoff of 100 Ry. The atomic structure of Bi/SiC in the calculations is based on experiments (18), where one unit cell of bismuthene is commensurate with a $\sqrt{3} \times \sqrt{3}$ supercell of the SiC (0001) surface with a lattice constant of 5.35 Å. The internal atomic positions are relaxed until the residual force on each atom is less than 0.01 eV/Å. We use one layer of SiC to mimic the substrate effect which is computationally achievable. The ab initio *GW* and *GW*-BSE calculations are performed using the BerkeleyGW package (35). We use a 2D truncation scheme and an energy cutoff of 30 Ry to compute the dielectric matrix for the screened Coulomb interaction. We sum up to 1,000 empty bands to calculate the self-energy to obtain the quasiparticle band structure. We perform *GW*-BSE calculations using two valence bands and two conduction bands. A $120 \times 120 \times 1\mathbf{k}$ grid of the Brillouin zone is used for the full-BZ calculations, and a patched sampling scheme with the sampling density equivalent to a $360 \times 360 \times 1\mathbf{k}$ grid of the BZ is used for the single-valley calculations for detailed analysis. More details are presented in *SI Appendix*.

Data, Materials, and Software Availability. All study data are included in the article and/or *SI Appendix*.

ACKNOWLEDGMENTS. This work was supported by the Theory of Materials Program at the Lawrence Berkeley National Laboratory (LBNL) through the Office of Basic Energy Sciences, U.S. Department of Energy under Contract No. DE-AC02-05CH11231, which provided the theoretical formulation and the GW and GW-BSE calculations. Advanced code developments were provided by the Center for Computational Study of Excited-State Phenomena in Energy Materials (C2SEPEM) at LBNL, which is funded by the U.S. Department of Energy, Office of Science, Basis Energy Sciences, Materials Sciences and Engineering Division under Contract No. DE-AC02-05CH11231, as part of the Computational Materials Sciences Program. Computational resources were provided by National Energy Research Scientific Computing Center, which is supported by the Office of Science of the US Department of Energy under contract no. DE-AC02-05CH11231, Stampede2 at the Texas Advanced Computing Center (TACC), The University of Texas at Austin through Extreme Science and Engineering Discovery Environment, which is supported by NSF under grant no. ACI-1053575 and Frontera at TACC, which is supported by the NSF under grant no. OAC1818253. We thank Q. Li, Z. Zhang, M. Wu, and T. Cao for helpful discussions.

Author affiliations: [a]Department of Physics, University of California at Berkeley, Berkeley, CA 94720; and [b]Materials Sciences Division, Lawrence Berkeley National Laboratory, Berkeley, CA 94720

Author contributions: J.R. and S.G.L. designed research; S.G.L. directed research; J.R. performed research; J.R., Z.L., C.S.O., and S.G.L. analyzed data; and J.R., Z.L., C.S.O., and S.G.L. wrote the paper.

1. M. L. Cohen, S. G. Louie, *Fundamentals of Condensed Matter Physics* (Cambridge University Press, 2016).
2. G. Wang *et al.*, Colloquium: Excitons in atomically thin transition metal dichalcogenides. *Rev. Modern Phys.* **90**, 21001 (2018).
3. X. Li *et al.*, An all-optical quantum gate in a semiconductor quantum dot. *Science* **301**, 809–811 (2003).
4. S. M. De Vasconcellos, S. Gordon, M. Bichler, T. Meier, A. Zrenner, Coherent control of a single exciton qubit by optoelectronic manipulation. *Nat. Photon.* **4**, 545–548 (2010).
5. E. Poem *et al.*, Optically induced rotation of an exciton spin in a semiconductor quantum dot. *Phys. Rev. Lett.* **107**, 087401 (2011).
6. T. Cao *et al.*, Valley-selective circular dichroism of monolayer molybdenum disulphide. *Nat. Commun.* **3**, 1–5 (2012).
7. D. Xiao, G.-B. Liu, W. Feng, X. Xu, W. Yao, Coupled spin and valley physics in monolayers of MoS 2 and other group-VI dichalcogenides. *Phys. Rev. Lett.* **108**, 196802 (2012).
8. K. F. Mak, D. Xiao, J. Shan, Light–valley interactions in 2D semiconductors. *Nat. Photon.* **12**, 451–460 (2018).
9. A. M. Jones *et al.*, Optical generation of excitonic valley coherence in monolayer WSe 2. *Nat. Nanotechnol.* **8**, 634–638 (2013).
10. X. Xu, W. Yao, D. Xiao, T. F. Heinz, Spin and pseudospins in layered transition metal dichalcogenides. *Nat. Phys.* **10**, 343–350 (2014).
11. G. Wang *et al.*, Control of exciton valley coherence in transition metal dichalcogenide monolayers. *Phys. Rev. Lett.* **117**, 187401 (2016).
12. G. Aivazian *et al.*, Magnetic control of valley pseudospin in monolayer WSe2. *Nat. Phys.* **11**, 148–152 (2015).
13. Z. Ye, D. Sun, T. F. Heinz, Optical manipulation of valley pseudospin. *Nat. Phys.* **13**, 26–29 (2017).
14. K. S. Novoselov, A. Mishchenko, A. Carvalho, A. H. Castro Neto, 2D materials and van der Waals heterostructures. *Science* **353**, acc9439 (2016).
15. A. K. Geim, I. V. Grigorieva, Van der Waals heterostructures. *Nature* **499**, 419–425 (2013).
16. N. P. Wilson, W. Yao, J. Shan, X. Xu, Excitons and emergent quantum phenomena in stacked 2D semiconductors. *Nature* **599**, 383–392 (2021).
17. T. H. Choudhury, X. Zhang, Z. Y. Al Balushi, M. Chubarov, J. M. Redwing, Epitaxial growth of two-dimensional layered transition metal dichalcogenides. *Annu. Rev. Mat. Res.* **50**, 155–177 (2020).
18. F. Reis *et al.*, Bismuthene on a SiC substrate: A candidate for a high-temperature quantum spin Hall material. *Science* **357**, 287–290 (2017).
19. M. Zhou *et al.*, Epitaxial growth of large-gap quantum spin Hall insulator on semiconductor surface. *Proc. Natl. Acad. Sci. U.S.A.* **111**, 14378–14381 (2014).
20. C.-H. Hsu *et al.*, The nontrivial electronic structure of Bi/Sb honeycombs on SiC (0001). *New J. Phys.* **17**, 025005 (2015).
21. M. Syperek *et al.*, Observation of room temperature excitons in an atomically thin topological insulator. *Nat. Commun.* **13**, 1–7 (2022).
22. M. S. Hybertsen, S. G. Louie, Electron correlation in semiconductors and insulators: Band gaps and quasiparticle energies. *Phys. Rev. B* **34**, 5390 (1986).
23. G. Li *et al.*, Theoretical paradigm for the quantum spin Hall effect at high temperatures. *Phys. Rev. B* **98**, 165146 (2018).
24. G. Xu, T. Zhou, B. Scharf, I. Žutić, Optically probing tunable band topology in atomic monolayers. *Phys. Rev. Lett.* **125**, 157402 (2020).
25. M. Rohlfing, S. G. Louie, Electron-hole excitations in semiconductors and insulators. *Phys. Rev. Lett.* **81**, 2312 (1998).
26. M. Rohlfing, S. G. Louie, Electron-hole excitations and optical spectra from first principles. *Phys. Rev. B* **62**, 4927 (2000).
27. M. M. Denisov, V. P. Makarov, Longitudinal and Transverse Excitons in Semiconductors. *Phys. Status Solidi (b)* **56**, 9–59 (1973).
28. T. Cao, M. Wu, S. G. Louie, Unifying optical selection rules for excitons in two dimensions: Band topology and winding numbers. *Phys. Rev. Lett.* **120**, 087402 (2018).
29. X. Zhang, W.-Y. Shan, D. Xiao, Optical selection rule of excitons in gapped chiral fermion systems. *Phys. Rev. Lett.* **120**, 077401 (2018).
30. L. Ju *et al.*, Tunable excitons in bilayer graphene. *Science* **358**, 907–910 (2017).
31. X.-X. Zhang *et al.*, Zeeman-induced valley-sensitive photocurrent in monolayer MoS 2. *Phys. Rev. Lett.* **122**, 127401 (2019).
32. L. Xie, X. Cui, Manipulating spin-polarized photocurrents in 2D transition metal dichalcogenides. *Proc. Natl. Acad. Sci. U.S.A.* **113**, 3746–3750 (2016).
33. M. Massicotte *et al.*, Dissociation of two-dimensional excitons in monolayer WSe 2. *Nat. Commun.* **9**, 1–7 (2018).
34. P. Giannozzi *et al.*, QUANTUM ESPRESSO: A modular and open-source software project for quantum simulations of materials. *J. Phys. Condens. Matter* **21**, 395502 (2009).
35. J. Deslippe *et al.*, BerkeleyGW: A massively parallel computer package for the calculation of the quasiparticle and optical properties of materials and nanostructures. *Comput. Phys. Commun.* **183**, 1269–1289 (2012).